Combined Remote Sensing Methods for Active Charge Control Using an Electron Beam in a Dynamic Space Environment

James D. Walker III*, Sebastian K. Hampl†
and Hanspeter Schaub‡
University of Colorado Boulder, Boulder, Colorado 80303

Active charge control of a target object allows a servicing spacecraft to control the electrostatic forces and torques experienced by the neighboring crafts. Driving the potentials to zero eliminates these perturbations for safer proximity and rendezvous operations while maintaining non-zero potentials yields non-contract forces, allowing the servicer to manipulate the motion of the target. The latter is interesting as a servicer with the ability to contactlessly move target objects is extremely beneficial for active debris removal. Closed loop control of a target's potential and methods for remotely sensing a target's electrostatic potential (the Secondary Electron and X-ray Methods) have been investigated, but only preliminary work has integrated both methods together. While prior work demonstrates offline sensing methods, this paper develops a new method for sensing a target's potential that is suitable for real-time potential measurements. The solution is demonstrated in active charge control vacuum chamber experiments. It is shown that, for this new Dual Method, by using the X-ray Method to inform the secondary electron method, quick and accurate potential control is achieved, combining the positive attributes of the two methods. Vacuum ultra-violet lights are also used to apply a constant current bias and evaluate both the controller and remote sensing methods in a non-ideal and dynamic charging environment. The inclusion of this photo-electron current is shown to not alter the ability of the control to converge, but does affect beam energies required to achieve a specific target potential.

I. Introduction

SPACECRAFT charging occurs when a conducting spacecraft is exposed to the energetic plasma of the space environment. As electrons, protons, and photons impact the surface, the potential of spacecraft deviates from that of the surrounding plasma. This potential depends on the region of space the satellite is traversing: low Earth orbit (LEO) satellites typically travel in a high density, low energy plasma, resulting in volt-level potentials [1]. Geostationary regions consist of low density, high energy plasma that allows spacecraft to charge between a few volts positive to ten's of kilovolts negative [1, 2]. Cislunar orbits experience a wide variety of plasma environments as the Moon orbits through different regions of Earth's magnetosphere: the space environment can range from the direct solar wind to the sparse magnetosphere lobes [3]. The work presented in this paper is most applicable to low density plasmas where the Debye lengths of the spacecraft (a measure of spacecraft's electrostatic influence) extends beyond tens of meters, such as in geostationary orbit (GEO) and cislunar space [4–6]. This allows nearby charged spacecraft to interact with one another, as opposed to in LEO where Debye lengths are on the order of centimeters [7].

In regions where the Debye length is small, the concerns that arise due to the non-neutral potentials include electrostatic discharges (ESDs) between components [1, 8] and measurement interference of sensitive plasma measurements [9, 10]. ESDs typically occur due to differential charging: the spacecraft surface is not fully conducting and disconnected components acquire different potentials. On the other hand, measurement interference can occur for nearly any charged spacecraft. If a spacecraft is charged to +10 V, any proton or ion with less than 10 eV of energy cannot penetrate the electric field of the spacecraft and therefore will not be measured. This leads to populations of low energy ions remaining hidden from spacecraft sensors [11]. In addition, any electron will be accelerated by the electric field, causing the particle energy to be measured 10 V greater. An estimation of the spacecraft potential can be used to adjust measured

---

*NDSEG Fellow and Graduate Research Assistant, Ann and H.J. Smead Department of Aerospace Engineering Sciences, University of Colorado Boulder, Colorado Center for Astrodynamics Research, Boulder, CO, 80303 USA. James.WalkerIii@colorado.edu

†Graduate Research Assistant, Ann and H.J. Smead Department of Aerospace Engineering Sciences, University of Colorado Boulder, Colorado Center for Astrodynamics Research, Boulder, CO, 80303 USA.

‡Distinguished Professor and Department Chair, Schaden Leadership Chair, Ann and H.J. Smead Department of Aerospace Engineering Sciences, Colorado Center for Astrodynamics Research. AAS Fellow, AIAA Fellow

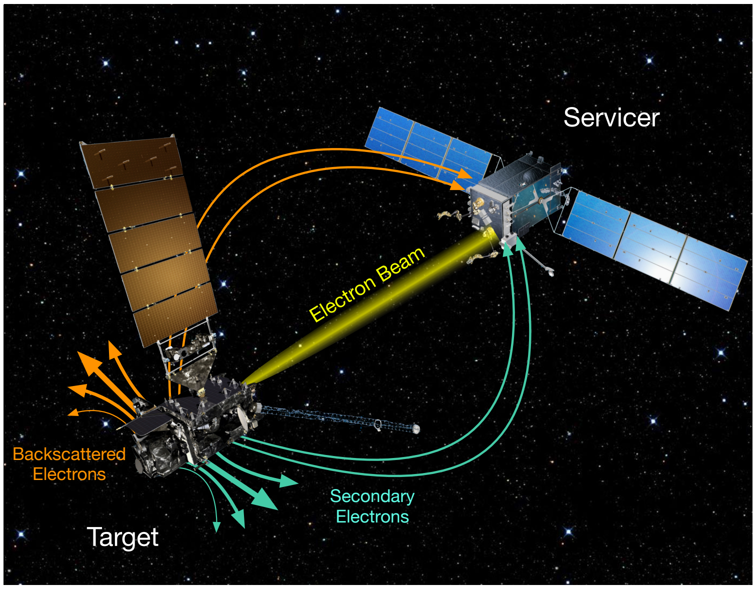

Fig. 1 An illustration of active charge control of an uncontrolled target [31].

potentials, but charge mitigation techniques must be employed to measured the "hidden ion population" [11]. When nearby spacecraft charge within each other's Debye length, additional concerns arise. ESD's can occur between the two craft during docking operations and electrostatic forces and torques are generated between charged objects [12–14]. When spacecraft are sufficiently close (meters to tens of meters), they become significant perturbations [14–16].

Techniques for mitigating charge have been developed and employed in situ. Energetic particle beams have been used to emit charged particles from spacecraft [17–20]. Through the emission of charge, a spacecraft applies a current to itself, allowing it to actively control its own potential. This phenomenon was first explored in situ by ATS 5 and 6 [17, 19] and has further been investigated and utilized on missions such as GeoTail, Cluster, and MMS [10, 21, 22]. Electron, ion, and neutral plasma emitters have all been used in situ to manipulate a spacecraft's potential, with ion and plasma emitters proving to be most effective [17, 19]. Because the current of the plasma emitters are controlled, often based on a measurement of the target's potential, these are active control methods. Passive charge mitigation methods have also been explored. Most of these methods either prevent plasma from impacting the spacecraft or emit charge as quickly as it accumulates [23]. Encasing conducting components with conducting grids and applying a large potential repels environmental plasma and prevents impacts [23]. High secondary electron yield (SEY) materials prevent a significant negative current to be generated and sharp, needle-like protrusions utilize field emission to emit charge as it accumulates [23]. Active charge control techniques have been shown to be very effective for maintaining near-neutral potentials on spacecraft, and have consequently seen significant usage in space, including on the international space station [24–26], but do require a measure of the spacecraft's potential. A controlled spacecraft can measure its own potential using a variety of instruments, including retarding potential analyzers (RPAs) [27], electron spectrometers [28], and conducting probes [29, 30].

Active charge control (ACC) has mainly been investigated for a spacecraft controlling its own potential. Proximity, rendezvous, and docking operations, would benefit from being able to control the potential of a nearby target object. Active debris removal (ADR) would be particularly affected by this development. Most proposed ADR techniques require physical contact with the debris object, such as the claw, harpoon, or net methods [32–36]. However, physical ADR techniques have concerns with complicated dynamics and generating additional debris. Aside from reducing electrostatic perturbations and ESD risks, ACC facilitates contactless debris removal: the electrostatic tractor (ET) harnesses spacecraft charging to "tug" defunct spacecraft to graveyard orbits [37, 38]. A controlled servicing spacecraft directs a beam of high energy electrons at the uncontrolled debris object. The incoming current charges the target negative while the emission of the negative particles charges the servicer positive. These opposite charges generate an attractive Coulomb force between the two objects. Using this non-contact force, the servicer is able to manipulate the motion of the debris [38]. Prior work found that a multi-ton debris object can be re-orbited in a matter of months using this concept [39].

In order to employ the electrostatic tractor, and charge mitigation of an uncontrolled target, the servicer must be able to control its own potential, measure the target's potential, and control the target's potential. The ability to control a servicer's potential in situ has already been discussed. Two methods for contactlessly measuring a target's electrostatic potential have been developed: the X-ray Method and the Secondary Electron Method (SEM). Both these techniques utilize a spacecraft equipped with a high energy electron gun exciting secondary electrons and x-rays from the target's surface and measuring their energies [40, 41]. Additionally, both techniques have been validated in vacuum chamber experiments. The details of these methods are discussed in further detail in Section IV. Finally, a servicing spacecraft must be able to control the potential of the uncontrolled target. Prior work investigating these operations has assumed control over a target's potential is possible, but actual techniques for achieving this have only recently been explored [42–44]. Reference 31 develops a proportional control adjusting the energy of an electron beam directed at a target. This control is proven to be stable for small deviations about the equilibrium location and validated using vacuum chamber experiments. However, this implementation of target ACC required an electrostatic voltmeter (Trek probe), a specialized tool for measuring a target's electrostatic potential. Integrating remote sensing methods into active charge control is the next step in advancing target ACC and the focus of this paper. The SEM has been implemented in closed loop control form [45]; however, its current implementation is inefficient and impractical. As such, more work must be conducted to properly integrate remote sensing methods.

The goal of this paper is to implement remote sensing techniques in an efficient and accurate manner by combining the X-ray Method and SEM. More specifically, the X-ray Method is used to "seed" the Secondary Electron Method. The X-ray Method is faster and has larger measurement range while the SEM is more accurate and more consistent. By integrating the methods together, the positive attributes of both can be achieved in a single technique. A comparison between this new method and the previous methods is conducted to demonstrate its advantages.

This paper also expands the robustness of the control outlined in Ref. 31 by evaluating the performance when exposed to an additional photo-electron current. Previous analysis and experiments only consider the currents induced by the electron beam. This novel investigation explores both the controller and remote sensing techniques in a static and dynamic charging environment caused by the photo-electron current. This the first investigation of these methods in a non-ideal charging environment.

The paper is organized in the following sections: Sec. II presents the relative background for spacecraft charging as well as an overview of the ACC controller. Next, the experimental setup used in this project is outlined in Sec. IV as well as a description of the each of the remote sensing methods employed in this work. Finally, the experimental results are presented in Sec. V. Sec. V includes a comparison between the previous remote sensing implementation to the new Dual Method, demonstrating its increased speed and accuracy. The controller is then evaluated in a dynamic environment, followed by an analysis of the behavior of each remote sensing method operating under these conditions.

II. Review of Numerical Charging Models

Experiments are conducted in a vacuum chamber environment with significant currents induced by an electron beam and a vacuum ultra-violet (VUV) lamp. There are no other environmental currents acting on the object. The overview of spacecraft charging presented here is derived from Ref. [1].

The first current acting on the target is the negative current induced by the electron gun, I_{EB}, and is described as

$$I_{\text{EB}}(\phi_T) = -\alpha I_{EM} \qquad \phi_S - \phi_T < E_{\text{EB}} \tag{1a}$$

$$I_{\text{EB}}(\phi_T) = 0 \qquad \phi_S - \phi_T \geq E_{\text{EB}}. \tag{1b}$$

Here, I_{EM} is the current emitted from the gun, ϕ_S and ϕ_T are the potential of the servicer and target respectively, and E_{EB} is the energy of the electron beam. The parameter α is used to describe the area of the electron beam impacting the target. For these experiments, the impact of the electron is calibrated such that the entire beam impacts the target and $I_{\text{EB}} = I_{EM}$ ($\alpha = 1$). Equation (1) is a piecewise function that depends on the spacecraft potentials and beam energy. When the energy of the electron beam is less than the difference between the two craft, the electrons are not energetic enough to reach the target and the resulting current is zero. Otherwise, the electrons are able to impact and apply a negative current to the target. The electron gun is grounded to the chamber such that $\phi_S = 0$ so the function simplifies to just target potential and beam energy.

While the electron gun directly applies a negative current, it also causes electrons to be emitted from the target, generating two additional positive currents through secondary and backscattered electrons. Secondary electrons are generated when a primary electron (the electron beam electron) impacts a surface and excites surface electrons on the target. These excited electrons can then be emitted from the surface as a secondary electron. Depending on the

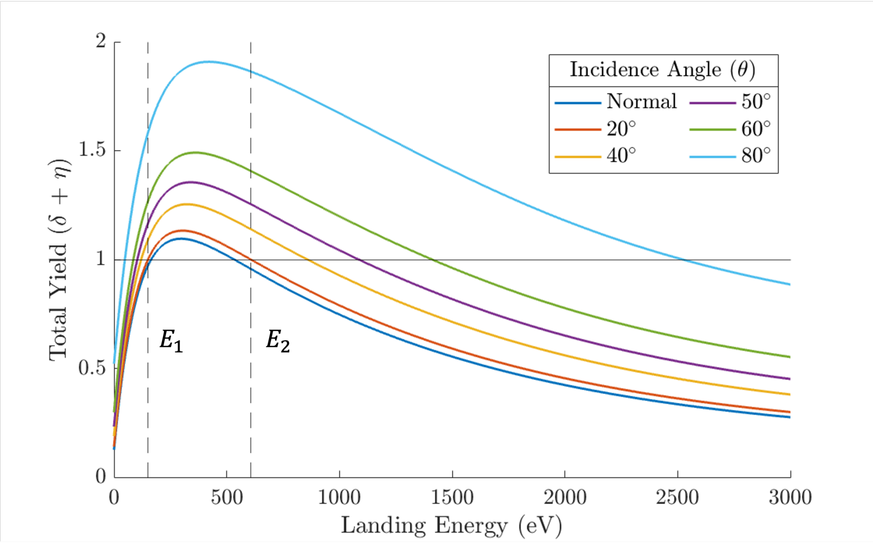

Fig. 2 Computed secondary electron yield for pure aluminum at variety of impact angles based on Refs. [48, 50, 51]

amount energy deposited by the primary electron, more than one secondary electron can be emitted. One electron is absorbed by the surface while two (or more) or emitted, resulting in the electron beam generating a positive current. This current directly depends on the current impacting the target and the secondary electron yield (SEY), $\delta(E)$, which is the probability of a secondary electron being emitted where the electron impact energy E is equal to the sum of the beam energy and target potential $E = E_{\text{EB}} + \phi_T$. The current due to secondary electrons is defined as

$$I_{\text{SEY}} = \delta(E) I_{\text{EB}}. \tag{2}$$

The SEY depends on the properties of the target surface including composition, contamination layers, and surface roughness [46, 47]. There are multiple methods for computing $\delta(E)$; the formula used in this paper was developed by Sanders and Inouye [48]. Using this model, $\delta(E)$ is computed as

$$\delta(E) = c\left[\exp\left(\frac{-E}{a}\right) - \exp\left(\frac{-E}{b}\right)\right], \tag{3}$$

where a, b and c are defined by $a = 4.3E_{\max}$, $b = 0.367E_{\max}$, and $c = 1.37\delta_{\max}$ [48]. The material properties $\delta_{\max}$ and $E_{\max}$ are the maximum yield and the energy at which the max yield occurs, respectively.

The other positive current is induced by backscattered electrons. As a primary electron approaches the target surface, it can be reflected, or backscattered away. Because of this, the electron never actually impacts the target surface and the backscattered electron is the same as the original primary electron. This current similarly depends on the current impacting the target and the backscattered electron yield (BEY), $\eta(E)$:

$$I_{\text{BEY}} = \eta(E) I_{\text{EB}} = (A - B\exp(-CE))\, I_{\text{EB}}. \tag{4}$$

Here, the model developed by Prokopenko and Laframboise is implemented and the material properties are A, B and C [49]. Unlike the SEY, because the impacting and backscattered electron are the same, the BEY can never exceed one. In fact, $\eta(E)$ is typically much smaller than one and almost constant for all E [23]. Both the secondary and backscattered currents depend on E, so δ and η are often summed together to get TEY, the total electron yield.

It is important to note that $\delta(E)$ and $\eta(E)$ also have an angular dependence. These yield values change if the electrons impact with a non-normal incidence angle [1]. Equations (2) and (4) are for normal incidence angle ($\delta(E, 0)$ and $\eta(E, 0)$). The angular dependent TEY equations are

$$\delta(E, \theta) = \delta(E, 0)\exp\left[\beta_s(E)(1 - \cos(\theta))\right] \tag{5a}$$

$$\eta(E, \theta) = \eta(E, 0)\exp\left[\beta_b(E)(1 - \cos(\theta))\right] \tag{5b}$$

where θ is the impact angle of the electrons [50] and β_s and β_b are determined in Ref. 51 as

$$\beta_s(E) = \exp(\zeta) \tag{6a}$$

$$\beta_b(E) = 7.37Z^{-0.56875} \tag{6b}$$

$$\zeta = 0.2755(\xi - 1.658) - \left([0.2755(\xi - 1.658)]^2 + 0.0228\right)^{0.5} \tag{6c}$$

$$\xi = \ln(E/E_{\max}). \tag{6d}$$

A non-normal incidence angles increases the TEY as shown by Fig. 2. For the experiments conducted in this paper, the target object is at an 18$^{\text{o}}$ angle with respect to the electron beam, meaning the change in TEY should be small and have minimal effect on the final results. However, it is an important aspect to consider as active charge control is further explored.

So far, only the currents generated by the electron beam have been presented, but to explore a dynamic charge environment, an environmental current must be included. When an energetic photon impacts an electron, it can be absorbed, moving the electron to an excited state. If enough energy is absorbed, the electron will be emitted from the material and repelled away, generating a positive current on the target. This photo-electron current is described by

$$I_{\text{ph}}(\phi) = j_{ph,0}A_{\perp}e^{-\phi/T_{ph}} \qquad \phi > 0 \tag{7a}$$

$$I_{\text{ph}}(\phi) = j_{ph,0}A_{\perp} \qquad \phi \leq 0, \tag{7b}$$

with $A_{\perp}$ being the cross-sectional area exposed to the light, T_{ph} being the temperature of emitted photo-electrons, and $j_{ph,0}$ being the photo-electron flux [1]. Photo-electrons are emitted with low energy (<10 eV), therefore, if the target potential increases above +10 V, photo-electrons will be attracted back to the target; no net charge is applied and the target maintains a weakly positive potential. For the work presented here, it is assumed that $\phi \leq 0$; therefore the photo-electron current will be a constant value.

Combining these equations gives the net current acting on the target:

$$I_{\text{net}} = -I_{\text{EB}} + \delta(E)I_{\text{EB}} + \eta(E)I_{\text{EB}} + I_{\text{ph}}. \tag{8}$$

Conducting spacecraft charge based on the Ohm's law:

$$\frac{\mathrm{d}\phi(t)}{\mathrm{d}t} = \frac{I_{\text{net}}(t)}{C_{\text{sc}}} = \frac{1}{C_{\text{sc}}}\left[-I_{\text{EB}}\left(\delta(E) + \eta(E) - 1\right) + I_{\text{ph}}\right], \tag{9}$$

where capacitance of the spacecraft C_{sc} is assumed to be constant. Therefore, the change in net current determines the charging behavior of the object. Charging continues until the target potential reaches an equilibrium point. At this point, the net current acting on the target is zero, the target potential remains constant, and the corresponding target potential is the *floating potential*.

III. Active Charge Control and Stability

The goal of target ACC is to manipulate the parameters of the electron beam to influence the electrostatic potential of the target. From Eq. (9), the relevant electron beam parameters are I_{EB} and in E_{EB}. Applying control to either of these parameters allows the servicing spacecraft to control the potential of the target object. Reference 31 shows that the electron beam energy control method is more effective than current control method. As such, the electron beam energy control method is employed here. The current of the electron beam is held constant during experiments. An overview of the analytical relationships of ACC and the stability analysis is provided next [31].

First, the differential equation describing the charging behavior of the target relative to the electron beam parameters must be determined. Taking Eq. (9), the term $(\delta(E) + \eta(E) - 1)$ is determined by the electron beam energy and TEY. Initially ignoring the I_{ph} term, a TEY < 1 means the target will charge negative while a TEY > 1 will charge the target positive. When TEY = 1, $\frac{\mathrm{d}\phi(t)}{\mathrm{d}t}$ is 0 and the target's potential is at equilibrium. By adjusting the energy of the electron beam, the TEY can be increased/decreased such that this equilibrium can be achieved. Fig. 2 shows that there are two such equilibrium points, E_1 and E_2. Graphically, it can be seen that the second crossover point, E_2 is a stable equilibrium while E_1 is unstable. This can also be shown analytically. Taking Eq. (9) as $f(E)$, plugging in each of the individual current equations, and taking the derivative with respect to E, $f'(E)$ is found to be

$$f'(E) = \frac{I_{EB}}{C_{\text{sc}}}\left[c\left(-\frac{e^{-\frac{E}{a}}}{a} + \frac{e^{-\frac{E}{b}}}{b}\right) + BCe^{-CE}\right]. \tag{10}$$

Evaluating $f'(E)$ at both of the equilibrium points gives the stability. Using the material properties for the experiments preformed in this paper, at E_1, the derivative is positive and the point is unstable. In contrast, at E_2, the derivative is negative, it is a stable equilibrium point. For most materials, $E_1 \approx 100\,\mathrm{eV}$. Using a beam energy of $E_{\mathrm{EB}} > 2\,\mathrm{keV}$ ensures that the system is operating around E_2.

The control implemented here utilizes this stable equilibrium: because the system will settle to E_2, the equilibrium potential can be found as $\phi_{T_{eq}} = E_2 - E_{\mathrm{EB}}$. The second crossover energy is constant for any given material, which means that, based on this relationship, changing the beam energy changes the target potential by the same amount. Energy ACC uses this principle to manipulate the beam energy such that $\phi_{T_{eq}} = \phi_G$, the goal potential of the control. It is important to note that, for this control to work, E_2 must exist. If the target material has a maximum TEY < 1 across all beam energies, a different control must be implemented.

Because electron beam energy and target potential have this direct relationship, a proportional controller is developed. This controller depends on the error in the target's potential relative to the goal potential:

$$u = K_P\left(\phi_{\mathrm{T}} - \phi_{\mathrm{G}}\right), \tag{11}$$

where K_P is the gain, ϕ_T is the measured potential of the target and ϕ_G is the goal potential of the control. This control has been proven to be stable for small deviations about the equilibrium of the system [31]. Defining the state vector as the target potential and the beam energy, the differential equation that governs energy active charge control can be written as

$$\dot{\mathbf{x}} = \begin{bmatrix} \dot{\phi}_T \\ \dot{E}_{\mathrm{EB}} \end{bmatrix} = \begin{bmatrix} \frac{I_{\mathrm{EB}}}{C_{\mathrm{sc}}}\left(\delta(E) + \eta(E) - 1\right) \\ 0 \end{bmatrix} + \begin{bmatrix} 0 \\ u \end{bmatrix} \tag{12}$$

again with

$$\begin{aligned} \delta(E) &= c\left[\exp\left(\frac{-(E_{\mathrm{EB}} + \phi_T)}{a}\right) - \exp\left(\frac{-(E_{\mathrm{EB}} + \phi_T)}{b}\right)\right] \\ \eta(E) &= A - B\exp(-C(E_{\mathrm{EB}} + \phi_T)). \end{aligned}$$

The equation is linearized about the desired goal potential and the beam energy required to achieve it. The system is also discretized. For realistic beam currents and target objects, the capacitance of the target is much smaller than the beam current (4-6 orders of magnitude). Because of this, the target charges to its equilibrium nearly instantly, which is maintained until the potential is measured and the control adjusted. This suggests that the system is closer to a discrete system. As such, the system is discretized with a zero order hold equal to the measurement time. The stability conditions of this linearized, discrete system is computed and found to reduce to

$$0 \leq K_P \leq 2. \tag{13}$$

These steps are shown in further detail in Ref. 31 where this analysis is originally presented. It is shown that the proportional controller is stable about the goal potential of the system when considering a target object irradiated by an electron beam in a vacuum chamber environment. This claim is significant as it was the first analysis of the active control of a target's electrostatic potential; however, this prior work considers charging in an idealized scenario. There are no disturbances or external currents. This is addressed in this section where an external photo-electron current is added to the stability analysis; this corresponds to a target in sunlit conditions in space.

The behavior of the target's potential is governed by Eq. (9) where I_{ph} is determined by Eq. (7) (and $\phi_T \leq 0$). With this additional current, the state equation of the system becomes

$$\dot{\mathbf{x}} = \begin{bmatrix} \dot{\phi}_T \\ \dot{E}_{\mathrm{EB}} \end{bmatrix} =$$

$$\begin{bmatrix} \frac{I_{\mathrm{EB}}}{C_{\mathrm{sc}}}\left(c\left[\exp\left(\frac{-(E_{\mathrm{EB}} + \phi_T)}{a}\right) - \exp\left(\frac{-(E_{\mathrm{EB}} + \phi_T)}{b}\right)\right] + A - B\exp\big(-C(E_{\mathrm{EB}} + \phi_T)\big) - 1\right) + \frac{j_{ph,0}A_{\perp}}{C_{\mathrm{sc}}} \\ 0 \end{bmatrix} + \begin{bmatrix} 0 \\ u \end{bmatrix}. \tag{14}$$

Following the same steps as Ref. 31, this nonlinear equation is linearized by preforming a Taylor series expansion about the goal state, $E_{\text{EB}} = E_{\text{G}}$ and $\phi_{\text{T}} = \phi_{\text{G}}$. This gives the linearized charging equations as

$$\delta\dot{\mathbf{x}} = \begin{bmatrix} \delta\dot{\phi}_T \\ \delta\dot{E}_{\text{EB}} \end{bmatrix} = \frac{I_{EB}}{C_{\text{sc}}} \begin{bmatrix} c\left(-\frac{e^{-\frac{E_2}{a}}}{a} + \frac{e^{-\frac{E_2}{b}}}{b}\right) + BCe^{-CE_2} & c\left(-\frac{e^{-\frac{E_2}{a}}}{a} + \frac{e^{-\frac{E_2}{b}}}{b}\right) + BCe^{-CE_2} \\ 0 & 0 \end{bmatrix} \begin{bmatrix} \delta\phi_{\text{T}} \\ \delta E_{EB} \end{bmatrix} + \begin{bmatrix} 0 \\ \delta u \end{bmatrix} \tag{15}$$

An important simplification at this step is that, at equilibrium, $E_{\text{G}} + \phi_{\text{G}} = E_2$. Now, the charging equation is in the form $\delta\dot{\mathbf{x}} = [A_{\text{m}}]\delta\mathbf{x} + [B_{\text{m}}]\delta u$. After this step, the $j_{ph,0}A_{\perp}$ term disappears and the photo-electron current does not appear in the linearized equations anymore. To linearize Eq. (14), the derivatives of the components of $[A]$ and $[B]$ must be taken with respect to the state vector components, ϕ_T and E_{EB}. Because I_{ph} does not depend on the state variables, the term drops out during the linearization. The photo-electron term disappears and Eq. (15) is identical to the linearized charging equation from Ref. 31, such that the resulting stability analysis will be the same.

The next step is to discretize the charging equation. The target charges significantly quicker than its potential can be measured and the electron beam energy adjusted. Between each measurement, control is constant, therefore, it acts as a discrete controller with a zero order hold over the time, Δt. Here, $\Delta t = 1$ to be consistent with the analysis from Ref. 31. To discretize the system, an augmented state matrix, $[\hat{A}]$ is constructed,

$$[\hat{A}] = \begin{bmatrix} [A] & [B] \end{bmatrix} = \begin{bmatrix} \beta & \beta & 0 \\ 0 & 0 & 1 \end{bmatrix} \tag{16}$$

such that

$$\delta\dot{\hat{\mathbf{x}}} = [\hat{A}] \begin{bmatrix} \delta\phi_{\text{T}} \\ \delta E_{\text{EB}} \\ \delta u \end{bmatrix} = [\hat{A}]\delta\hat{\mathbf{x}} \tag{17}$$

with

$$\beta = \frac{I_{EB}}{C_{\text{sc}}}\left(c\left(-\frac{e^{-\frac{E_2}{a}}}{a} + \frac{e^{-\frac{E_2}{b}}}{b}\right) + BCe^{-CE_2}\right). \tag{18}$$

The solution to Eq. (17) is a matrix exponential with respect to $[\hat{A}]\Delta t$,

$$e^{[\hat{A}]\Delta t} = \begin{bmatrix} [F] & [G] \\ 0 & 1 \end{bmatrix} = \begin{bmatrix} \begin{bmatrix} e^{\beta} & e^{\beta} - 1 \\ 0 & 1 \end{bmatrix} & \begin{bmatrix} -\frac{\beta - e^{\beta} + 1}{\beta} \\ 1 \end{bmatrix} \\ 0 & 1 \end{bmatrix} \tag{19}$$

which gives matrices $[F]$ and $[G]$, which are used to define the discrete system $\delta\mathbf{x}_{k+1} = [F]\delta\mathbf{x}_k + [G]\delta u_k$. Finding the eigenvalues of this system will determine its stability conditions. To do this, the δu_k must be converted into $\mathbf{x}_k$. Taking the gradient of Eq. (11) gives $\delta u_k = [K]\delta\mathbf{x}_k$ with $[K] = [K_P, 0]$. Plugging this back into the discrete system yields

$$\delta\mathbf{x}_{k+1} = [F]\delta\mathbf{x}_k + [G]\delta u_k = [F]\delta\mathbf{x}_k + [G][K]\delta\mathbf{x}_k = ([F] + [G][K])\delta\mathbf{x}_k. \tag{20}$$

For a discrete system to be stable, the eigenvalues of the system must be between -1 and 1, or $|\lambda| < 1$. The eigenvalues of this system are found to be

$$|\lambda| = \left| \frac{\beta - K_P - K_P\beta \pm \sqrt{4K_P\beta + (K_P - \beta + K_P\beta)^2}}{2\beta} \right| < 1. \tag{21}$$

Initially, it appears that this inequality will have a complicated solution, but there is a final simplification that can be implemented. As discussed in Ref. 31, β is a large, negative value for any realistic material. This is because β depends on $\frac{I_{\text{EB}}}{C_{\text{sc}}}$. For typical applications of this control, beam currents are relatively large at 100's of μA while the capacitance is around 0.1 nF. This gives a value on the order 10^6, meaning $|\beta| >> K_P$. Applying this to Eq. (21), the final stability condition becomes

$$0 \leq K_P \leq 2. \tag{22}$$

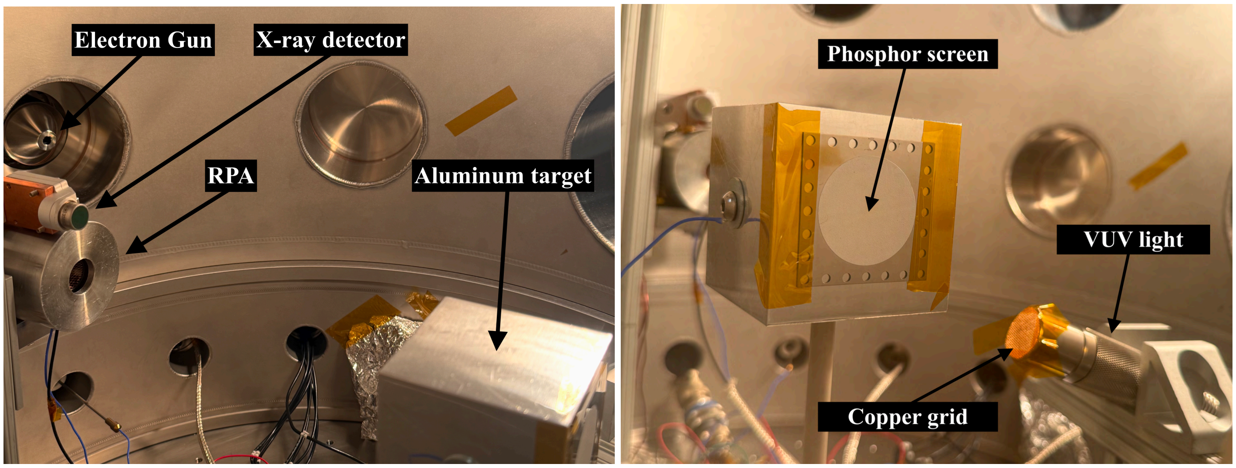

(a) (b)

Fig. 3 Experimental setup inside the ECLIPS vacuum chamber.

The same condition was derived when considering only electron beam currents are acting on the target [31]. Even though the resulting gain inequality is the same, there is one significant difference with this analysis. In order for this to hold, $I_{\mathrm{EB}} > I_{ph}$. If this is not the case, referring back to Eq. — and assuming a minimum TEY = 0 — then the target will always charge positive regardless of the beam energy and the control will fail to converge.

While this analysis is preformed only considering the photo-electron current, this stability condition will be true for any positive current that does not depend on the target potential or beam energy, as it will drop out during the linearization. This is a powerful result as it suggests that positive constant currents do not affect the gains required for stable control as long as the value of the bias is not greater than that of the electron beam current. The application of this result is that, for a spacecraft charging in sunlight, as long as a sufficiently large current can be applied, stable active charge control can be achieved on an uncontrolled target.

IV. Experimental Methods

A. Experimental Setup

Experiments are conducted in the Electrostatic Charging Laboratory for Interactions between Plasma and Spacecraft (ECLIPS) Vacuum Chamber at the Autonomous Vehicle Systems (AVS) laboratory at the University of Colorado Boulder. The experimental setup includes a high energy electron gun, retarding potential analyzer (RPA), x-ray detector, aluminum target, and a VUV lamp.

The high energy electron gun is a Kimball Physics EGPS-4212B with maximum beam current of 100 μA and energy range of 1-30 keV. For the experiments presented in this work, the beam current ranges between 5-13 μA and the energy range is 2–10 keV to ensure the nearby equilibrium point is E_2. Because TEY depends on the impact angle of the beam, a phosphor screen is used to ensure the impact location of the beam on the target is consistent across all beam energies. When exposed to energetic electrons, the surface of phosphor screen illuminates blue, allowing the impact location to be visually confirmed. For every beam energy in the operating range (in 500 eV increments), the beam deflection required to achieve the same impact location on the target is determined.

A 4 in × 4 in aluminum cube is used to simulate the spacecraft. The cube represents the shape of a spacecraft bus and aluminum is a commonly used material for satellites. The flat face the cube also makes the direction of the emitted secondaries more predictable, allowing for the RPA and x-ray detector to be accurately aligned. For the target used here, a layer of aluminum dioxide has built up due to prolonged exposure to the air. This surface contamination increases the TEY such that the secondary cross over energy is ≈ 2.5 keV as opposed to pure aluminum which does not cross TEY = 1.

To generate the positive photo-electron current, a Hamamatsu L10706-S2D2 VUV light source is used. This source has peak emissions at energies of 3.10 and 10.78 eV. With a work function of 4.08 eV, electrons will be emitted from the aluminum surface. Unlike the electron beam, control cannot be applied to the VUV lamp: it can only be turned on and off. For the electron beam current and energy range used in this paper, the photo-electron current generated by the unobstructed light is significantly larger than current applied by the electron beam which prevents charging at all tested beam currents. To account for this, a copper mesh with 36% open area is placed over the lamp. This reduces the impacting photons, allowing the target to charge negatively even with the additional current bias.

Finally, an RPA and x-ray detector are used to measure the particles excited from the target surface. An RPA is a gridded Faraday cup where the external grid is grounded and the voltage of the internal grid is varied. As electrons pass through the inlet, they pass through the grids and impact the collecting plate where the resulting current is measured. As the voltage of the internal grid increases, the incoming electrons are slowed down by its electric field. Once the voltage of the internal grid is greater than the electron energy, the electrons are not sufficiently energetic to penetrate through the electric field of the grid and are no longer measured. At this point, there is a steep drop off in measured current, indicating the energy of the impacting electrons. The x-ray detector used here is an Amptek 123 FAST SDD Ultra High Performance Silicon Drift Detector and has measurement range of 0-18.12 keV. This detector has a 0.5 mil thick beryllium window which window prevents high energy electrons from penetrating into the x-ray detector and being measured; however, the trade off is that low energy photons, < 0.9 keV, also cannot be measured. The region of interest for the obtained x-ray data is photons > 2keV, therefore this lack of data is not a concern.

B. Target Potential Remotely Sensing

In prior work, two methods for remotely sensing a target spacecraft's electrostatic potential have been developed; the SEM and X-ray Method. Both utilize a high energy electron beam impacting the target surface. For the SEM, secondaries are emitted with low energy (< 10 eV) and repelled away from the negatively charged target [52]. They impact the servicer with energy equal to the potential difference between the two spacecraft and are measured by the RPA. Knowing the potential of itself, the servicer is then able to estimate the potential of the target spacecraft [52]. Because the electron beam and RPA are grounded, the servicer potential is zero and the secondary electron impact the RPA with energy equal to the target's potential.

For the X-ray Method, when primary electrons impact the target surface, Bremsstrahlung radiation is also generated. As a primary electron approaches the negatively charged target it is accelerated by the electric field and impacts with an energy equal to the sum of the beam energy and target potential, minus the servicer's potential. During the impact, when the electrons interact with the target surface, they can be slowed down, releasing the lost energy as a photon, which can then be measured by the x-ray detector. The maximum photon energy corresponds to the maximum impact energy of the primary electron which is equal to $E_{\mathrm{ph}_{\mathrm{max}}} = E_{\mathrm{EB}} + \phi_T - \phi_S$ [41]. Determining the maximum photon energy and knowing the beam energy and servicer potential, the target potential can be estimated [41]. Again, the electron beam and RPA are grounded to the chamber walls so $\phi_s = 0$ and does not need to be accounted for.

Both of these sensing methods have been validated in vacuum chamber environments [41, 52] as a technique to measure the potential, but the solutions require post-processing of the sensor data. In practice, the SEM has greater max accuracy, about 20 V, and is more consistent in its measurements. But, the speed of the measurements relies heavily on the range and step size of the voltage sweep, typically resulting in long measurement times [52]. Additionally, the SEM can only measure potentials within its predefined voltage range. If a target is charged to -10 keV and the SEM voltage sweep is between 0 and -5 keV, the potential will not be accurately measured. The X-ray Method, on the other hand, can measure the entire sample space much faster. The actual range depends on the detector; however, the X-ray Method has a lower accuracy, in the range of 100s of volts [41]. This accuracy also decreases when measuring potentials close to zero where the error can approach up to ± 500 V [41]. The measurement consistency also relies heavily on the measurement of the noise floor, which can be inconsistent.

Dual Method Each of these methods, although they have been validated in vacuum chamber experiments and integrated into ACC, have significant concerns with the measurement accuracy/consistency or efficiency. To address these concerns, a new method for measuring a target's potential is developed here. The Dual Method is a novel method for measuring the target's potential that leverages the speed and range of the X-ray Method while achieving the accuracy and measurement consistency of the SEM. These advantages are realized by applying the two techniques sequentially, with the X-ray Method providing an initial estimate that guides the subsequent SEM measurement.

First, as part of the X-ray Method, the energy spectrum of the x-rays emitted from the target is collected. With the full spectrum, the characteristic peaks are removed and a linear line is fit to the resulting Bremsstrahlung spectrum. The intersection of the line of best fit and zero is determined and used to compute the estimated electric potential of the target [53]. One key factor in finding the linear fit is determining which data from the spectrum to use. In these experiments, the most significant source of noise is the detector itself, which must be characterized beforehand. In situ, a measurement can be taken without the electron beam on to determine the background noise caused by the environment. Any energy with photon counts below the noise floor is discarded. With noise removed from the spectrum, the zero crossing is determined from the linear fit. In practice, the final measurements are typically noisy and have errors up to 200 V. While this is relatively inaccurate, each x-ray measurement searches the entire range of the detector. This means the X-ray method takes the range of the possible values from 0-≈-18 kV to $\phi_{\text{x-ray}}\pm 200$ V. This provides a sufficiently good first estimate for the target's potential. To acquire the same result with the SEM, much longer and inefficient voltage sweeps must be conducted.

With a quick estimate of the target's potential, the next step is to improve the accuracy of the measurement with the SEM. The key to implementing the SEM is defining the bounds and step size of the voltage sweep. Using the X-ray Method estimate, $\phi_{\text{x-ray}}$, the bounds of the voltage sweep are defined by the error of 200 V. Specifically, the range is centered around $\phi_{\text{x-ray}}$ so the resulting upper bound is $\phi_{\text{x-ray}} + 200$ V and the lower bound is $\phi_{\text{x-ray}} - 200$ V giving a range of 400 V. The exact computation of the bounds depends on the characterization of the x-ray detector. With the range of the voltage sweep defined, the step size, V_s is next. The step size directly determines the accuracy of the final measurement. In this case, 20 V is chosen as, in practice, this is the smallest resolution that yields consistent measurements with the in house built RPA. The rest of the SEM is to determine the drop in measured current. Again, this requires some characterization of the RPA that must be preformed beforehand. However, the drop in current is typically around an order of magnitude difference between the currents at sequential grid voltages. With the grid voltage corresponding to the drop in current determined, the target's potential can be computed with an accuracy of V_s. This is the final value output from the Dual Method.

Even though two different methods are being used sequentially to obtain a single measurement, the small voltage sweep makes the SEM much faster. In fact, preforming both sensing methods sequentially is comparable in speed to only running the X-ray Method (and significantly faster than the unrefined SEM). This means, for a similar measurement time, a more accurate measurement can be achieved using the Dual Method instead of the X-ray method. This behavior is shown in the following section through ACC experiments where a measurement of the target's potential is obtained and used to inform the controller. Each of the three sensing methods are implemented experimentally and compared.

All sensing methods, as well as the control of the multimeters, power supplies, and motors used in these experiments, are implemented using LabVIEW.

V. Experimental Results

A. Floating Potentials

Before implementing charge control, the floating potentials of the target object are determined using both the X-ray Method and SEM. Using this data, the effect of the electron beam and the relationship between beam energy and target potential can be observed.

With the VUV lamp turned off and no photo-electron current, beam energy and target potential appear to have a relatively linear relationship. This is expected as, in theory, they should have a linear relationship with a slope of negative one: increasing the beam energy by 1 keV should decrease the target potential by 1 keV [1]. Additionally, it can be seen that increasing the electron beam current does not effect the final potential of the target. This can be seen in Eq. (III) (with $I_{\text{ph}} = 0$). This is expected as the equilibrium point is only determined by $\delta(E)$ and $\eta(E)$. With the VUV lamp turned on, the behavior changes.

First, there is clear shift in the floating potentials. In order for the currents to balance, the TEY can no longer be 1 as there must be a negative current to cancel the positive current. This means that at equilibrium, the TEY must be less than 1, increasing the beam energy required for equilibrium. This is seen as non-zero charging does not occur until the beam energy exceeds 5 keV, as opposed to 2.5 keV without the photo-electron current. The inclusion of the VUV lamps also changes the effect of I_{EB}: now, the amount of negative current impacting the target also affects the equilibrium. Decreasing I_{EB} means that the TEY must be lower in order for the currents to balance: increasing/decreasing the beam current will also shift the floating potentials. Decreasing I_{EB} excessively can result in the electron beam never charging the target if $|I_{\text{EB}}| < I_{\text{ph}}$, as can be seen when $I_{\text{EB}} = 5\mu$A with the VUV lamp on: the target does not charge at any beam energy. While this can be a concern for active charge control, it does open an interesting avenue for passive charge control.

If a spacecraft is equipped with a sufficiently strong VUV lamp, a large enough photo-electron current could be applied to a target such that the target never charges significantly. This would require the photo-electron current to be larger than the net environmental currents acting on the spacecraft. A target charged to near 0 V would eliminate

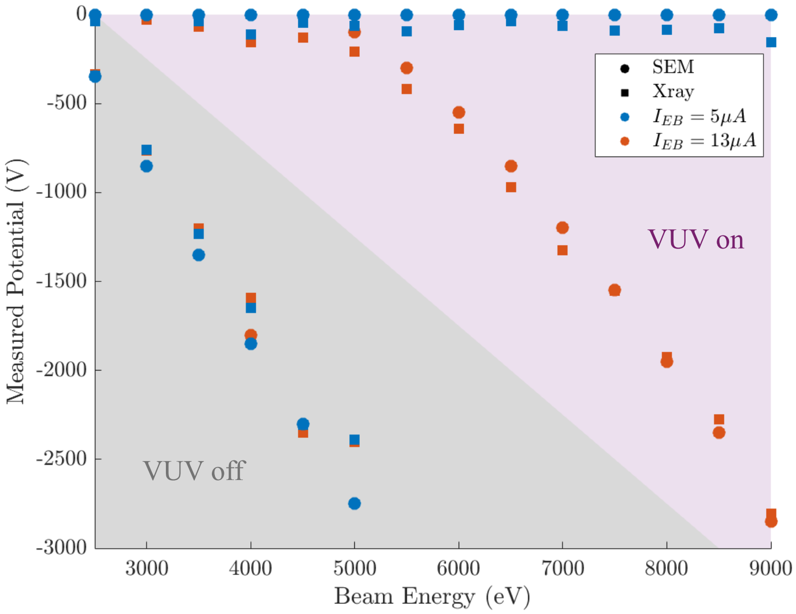

Fig. 4 The floating potentials measured using the SEM and X-ray method with and without a photo-electron current.

the electrostatic forces and torques the two spacecraft experience, removing electrostatic perturbations. Additionally, driving both the target and servicer potentials to near zero values would significantly reduce the concern of ESDs during docking operations.

B. Dual Method in a Vacuum Chamber Environment

The proportional control outlined in Sec. II is employed here. Fig. 5 shows two ACC trials using the Dual Method. Both trials start at 0 V (E_{EB_0} = 2 kV) and have a proportional gain of $K_P = 1$. This figure presents both the potential estimate from the X-ray method and the refined measurement from the SEM. In each case, the X-ray Method underestimates the target's potential compared to the SEM. This occurs due to the measurement noise the detector experiences. In order to determine the maximum photon energy, a line is fit to the x-ray spectrum and the zero crossing of the line is determined. When noise is present, the fit line is shifted and the max photon energy is measured higher than the actual value. A high maximum photon energy corresponds to a lower target potential (in magnitude). This effect can be mitigated with an accurate measurement of the noise floor and discarding data that falls below it. In these vacuum chamber experiments, the only significant source of noise is from the detector itself; for in situ applications, the environmental radiation is significantly larger and would be the driving source of noise. Collecting measurements without the electron beam turned on provides a measurement of the noise floor. This underestimation of target potential is also accounted for in the sweep of the SEM. In contrast to the description in Sec. IV, the voltage sweep used in experiments is chosen not to be symmetric around $\phi_{\text{x-ray}}$. Instead, the sweep is skewed negative with +100 V and -400 V as it is unlikely for the X-ray Method to overestimate the target's potential. This allows for a more efficient SEM to be preformed

It is clear that both trials are able to achieve the desired goal potentials of -2 keV and -4 keV. Each trial using the Dual Method was able to converge to the desired goal potential within a small error of 20 V. They also converge within a reasonable amount of time. The actual convergence times depend on the gain, but, for reasonable gain (around 1), each trial converges in 3-4 measurements. Both the X-ray method and refined SEM take about 60 s, meaning each measurement takes two minutes; however, this time can be reduced with higher quality and more specialized sensors.

All three sensing methods are shown in Fig. 6 for the same charging scenario, a target initially at 0 V with a goal potential of -2 kV and a proportional gain of 1. Initially comparing the SEM to the Dual Method, it is clear the Dual Method is significantly faster. Both methods take 3–4 measurements to fully converge, but each measurement of the

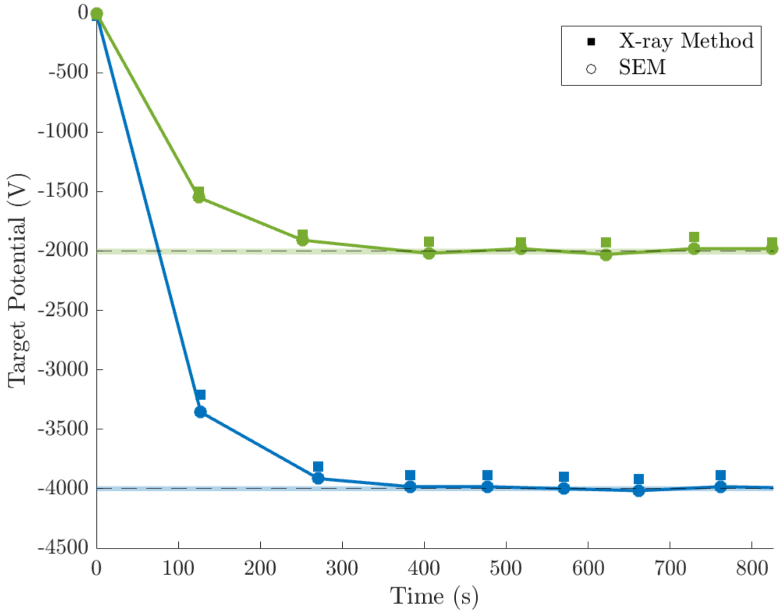

Fig. 5 Energy active charge control using the Dual Method for sensing.

SEM takes significantly longer. In fact, the Dual Method converges in about half the time of the SEM. This is because, in order to cover the entire experimental space with a small resolution, the voltage sweep of each measurement is from 0 to -4 kV with a step size of 50 V. With the small step size and large range, each measurement requires 101 steps, which leads to long measurement times. In contrast, because the SEM is seeded in the Dual Method, each measurement only has 26 steps. For this comparison, the step size of the Dual Method is more precise, 20 V, while that of the SEM is 50 V. Using the more refined voltage with the SEM require 251 steps. While the convergence times are significantly different, both methods achieve the same accuracy at steady state of 20 V. High quality instrumentation could be employed to increase the measurement times, but the SEM would still be very inefficient. To get an accurate measurement, only values at and around the target potential are required; all the other values from the SEM sweep are useless. The refined sweep of the Dual Method is a much more efficient use of the SEM.

Comparing the Dual Method and the X-ray Method, it is clear that, while the X-ray Method is faster, the speed of either technique is similar, with the Dual method converging after 400 s and the X-ray Method converging after 300 s. Additionally, a more accurate x-ray sensor would allow for the SEM range to be reduced, increasing the measurement speeds further. The consistency and accuracy of the SEM measurements is the big difference. After the X-ray Method has converged, the measured potential still fluctuates significant around -2 kV. For the Dual Method, the convergence is very stable with a max deviation of 20 V. While only one set of trials is shown here, the general behavior is consistent across all tested trials.

C. Active Charge Control in a Dynamic Space Environment

So far, target ACC work has only been explored in an ideal vacuum chamber environment. This has been useful for determining the relationship between beam energy and target potential, but now this work will be expanded to a more complex environment. In GEO, as a satellite emerges from eclipse, it transitions from a strongly negative environment to a weakly positive one. This can be simulated in a vacuum chamber using a VUV lamp. Figure 7 shows a single trial of ACC using the Dual Method with the VUV lamp turned on partway through, simulating a spacecraft coming out of Earth's shadow. This trial has a gain of 1, a goal potential of -1.5 kV, and a beam current of 10 μA.

The gray region corresponds to the section of the trial where the VUV lamps are turned off. The control is able to converge as expected with a final beam energy of $\approx$ 4.2 keV. At 640 s, the purple region, the photo-electron current is applied and the target immediately charges to a near zero value. It takes two more control instances and a beam energy $>$ 7 keV for charging to occur. Once the target begins charging again, the system converges to the desired potential in

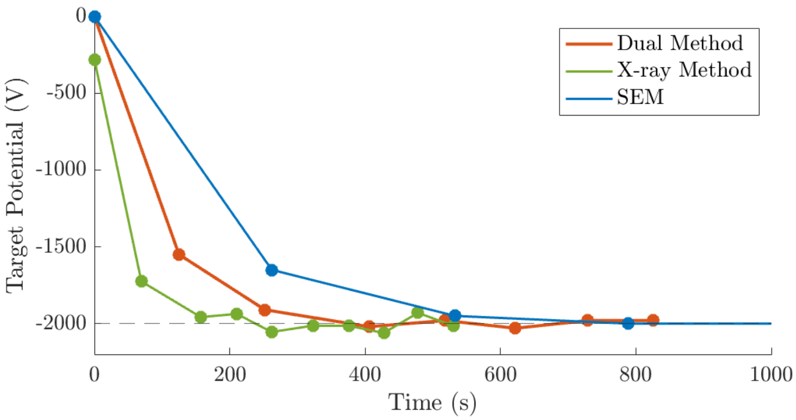

Fig. 6 Energy ACC with a $\phi_G = -2$ kV employing a variety of remote sensing methods.

three measurements. Interestingly, when the positive bias is included, $K_P = 1$ is no longer the optimal gain. Instead, it takes multiple measurements to get close to the goal potential. This occurs because the relationship between beam energy and target potential no longer has a slope of one. Including the positive bias appears to decrease the slope of this relationship, which in turn affects the optimal gain. The actual gain required for the control to converge is equal to $1/m$ where m is the slope of the relationship. Because the optimal gain changes, the stability conditions likely change as well, with the system being stable when gains exceed $K_P = 2$.

In Sec. II, it is shown that the positive bias does not change the stability conditions of the system as the constant term drops out in the linearization. However, because of the linearization , stability arguments can only be made for small deviations from the equilibrium point. This experimental trial has potentials that are a significant distance away (up to 100% deviation), where the linearized stability conditions may no longer hold. It is also possible that this unexpected behavior occurs because of the non-ideal nature of experiments. The aluminum target used in these experiments has seen extensive use and significant exposure to atmosphere, resulting in inconsistent surface properties. Total electron yield depends on these properties and is a driving property in ACC, which has caused similar behavior is previous work [31].

Finally, the SEM and X-ray Method are also implemented with the VUV light injection and compared to the Dual Method in Fig. 7. The trial shown in Fig. 8a shows the same charging scenario as Fig. 7 where a constant voltage sweep of 0 – -5 kV is used. The trial of the X-ray Method is not identical to that for the Dual Method and therefore a direct comparison cannot be made, however the general behavior can be compared: the difference is a goal of potential of -1.5 kV instead of -2 kV.

On first inspection, it can be seen that both sensing methods can be integrated to allow for accurate sensing in a dynamic environment. In Fig. 8b, the X-ray method is comparable in speed to the Dual Method, although it does require more measurements to converge. Moreover, the resulting measurement accuracy shown here is comparable to that of the SEM. This is an interesting result as highly accurate measurements can be achieved with only the X-ray method. However, these results are not consistent across all trials and more work is required to fully characterize the behavior. From Fig. 8a, the SEM has very similar behavior to the Dual Method, just with longer measurement times, but this will not always be the case. Using the SEM only, the range of potentials that can be measured depends on the range of the voltage sweep. In this experiment, the voltage sweeps between 0 and -5 kV, meaning potentials less than -5 kV cannot be accurately measured. This is a concern when the space environment suddenly becomes more negative, like during increased geomagnetic activity. The Dual Method is able to account for this with the x-ray measurements of the entire measurement space. Increasing the sweep of the SEM to fit the entire sample space, but this would lead to very long and inefficient control.

VI. Conclusion

The goal of this paper is to integrate electrostatic potential remote sensing methods into active charge control in a manner that allows for quick and accurate convergence. Both previoulsy proposed methods, the X-ray Method and Secondary Electron Method, can be integrated into ACC, but the resulting control is either fast but inaccurate, or accurate and slow. By combining these two methods into the Dual Method, quick and accurate convergence was

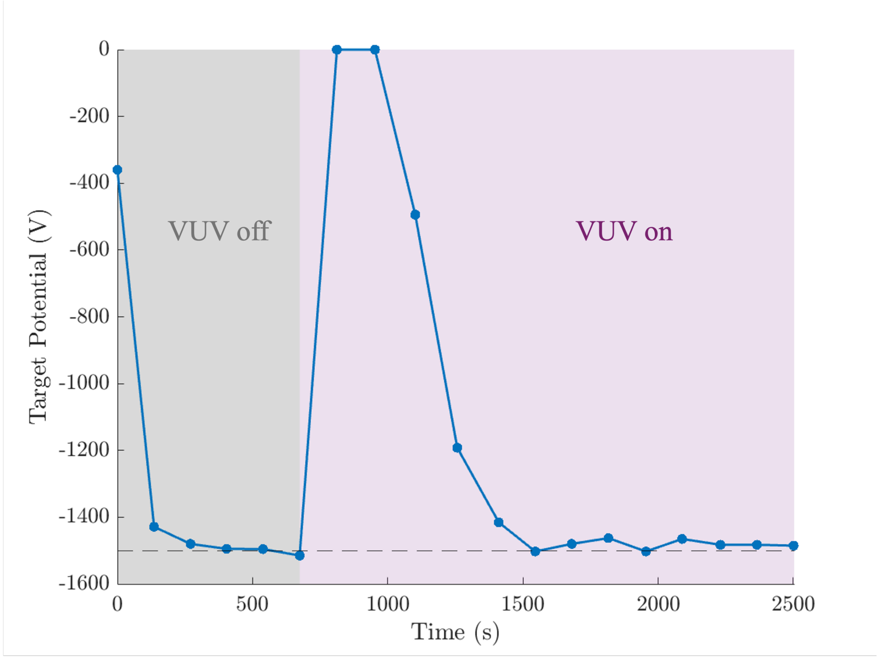

Fig. 7 Active charge control using the Dual Method with a photo-electron current injected in the middle of the trial.

achieved across all tested trials. The speed of each measurement is comparable to using only the X-ray Method while the control converges to the goal potential with the small error of the SEM.

This work also explores active charge control with an environmental current, specifically a positive photo-electron current. The analysis shows that this control is robust to a constant positive current as long as the magnitude of the electron beam current is larger than the bias. If this is not the case, the target will maintain a constant, weakly positive potential. While this is a concern for active charge control, this opens up opportunities for passively charging a target object.

This analysis is also supported by experimental trials. Using a VUV lamp to apply the photo-electron current, the electron beam control was able to achieve, and maintain, a desired potential on a floating target. Each of the remote sensing methods are explored in a simplified dynamic space environment as well. Convergence is achieved using each method, however, only the X-ray Method and Dual Method are able to accurately measure, and control, the target's potential in a dynamic environment, as the SEM relies on an unchanging voltage sweep. Ultimately, the best sensing method will depend on parameters and operating environment of the spacecraft, but this work highlights some of the benefits and limitations of these techniques that had previously never been explored.

Acknowledgments

This project was supported by the Department of Defense (DoD) through the National Defense Science and Engineering Graduate (NDSEG) Fellowship Program. Thank you to the Air Force Office of Scientific Research (AFOSR) for general support enabling Electrostatic Tractor research.

References

[1] Lai, S. T., *Fundamentals of Spacecraft Charging*, Princeton University Press, 2011. https://doi.org/10.2307/j.ctvcm4j2n.

[2] DeForest, S. E., "Spacecraft charging at synchronous orbit," *Journal of Geophysical Research (1896-1977)*, Vol. 77, No. 4, 1972, pp. 651–659. https://doi.org/https://doi.org/10.1029/JA077i004p00651.

[3] Halekas, J., Saito, Y., Delory, G., and Farrell, W., "New views of the lunar plasma environment," *Planetary and Space Science*, Vol. 59, No. 14, 2011, pp. 1681–1694. https://doi.org/https://doi.org/10.1016/j.pss.2010.08.011, URL https://www.sciencedirect.com/science/article/pii/S0032063310002497, lunar Dust, Atmosphere and Plasma: The Next Steps.

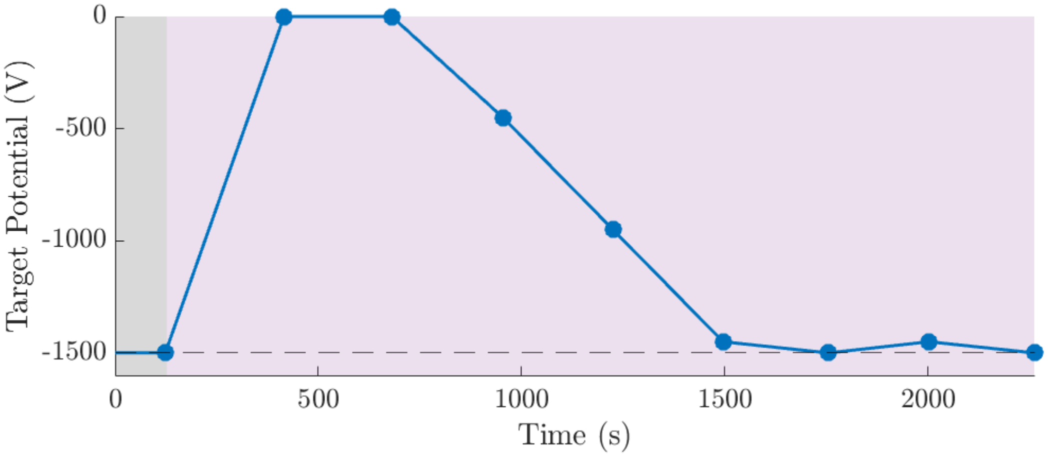

(a) Secondary Electron Method

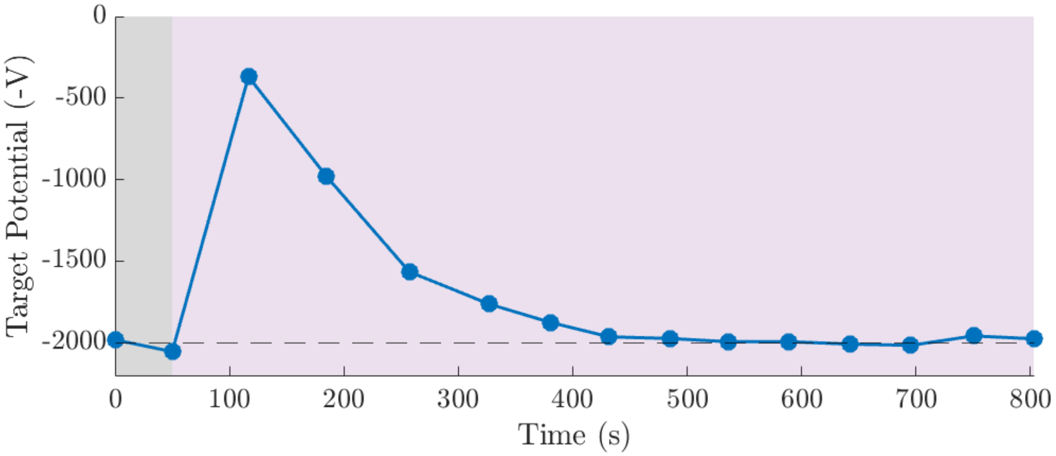

(b) X-ray Method

Fig. 8 Active charge control with an injected photo-electron current

[4] Seubert, C. R., Stiles, L. A., and Schaub, H., "Effective Coulomb force modeling for spacecraft in Earth orbit plasmas," *Advances in Space Research*, Vol. 54, No. 2, 2014, pp. 209–220. https://doi.org/10.1016/j.asr.2014.04.005.

[5] Denton, M. H., Thomsen, M. F., Korth, H., Lynch, S., Zhang, J. C., and Liemohn, M. W., "Bulk plasma properties at geosynchronous orbit," *Journal of Geophysical Research: Space Physics*, Vol. 110, No. A7, 2005. https://doi.org/10.1029/2004JA010861.

[6] Champion, K., and Schaub, H., "Electrostatic Potential Shielding in Representative Cislunar Regions," *IEEE Transactions on Plasma Science*, Vol. 51, No. 9, 2023, pp. 2482–2500. https://doi.org/10.1109/TPS.2023.3236246.

[7] Hastings, D. E., and Garrett, H. B., *Spacecraft–Environment Interactions*, Cambridge University Press, Cambridge, UK, 1996.

[8] Francis, C., "Electrostatic charging problems of spacecraft," *Journal of Electrostatics*, Vol. 11, No. 3, 1982, pp. 265–280. https://doi.org/10.1016/0304-3886(82)90017-1.

[9] Koons, H. C., and Gorney, D. J., "The Relationship between electrostatic discharges on spacecraft P78-2 and the electron environment," *Journal of Spacecraft and Rockets*, Vol. 28, No. 6, 1991, pp. 683–688. https://doi.org/10.2514/3.26300.

[10] Torkar, K., Nakamura, R., and Tajmar, M., "Active Spacecraft Potential Control Investigation," *Space Sci Rev*, 2016. https://doi.org/10.1007/s11214-014-0049-3.

[11] Olsen, R. C., "The hidden ion population of the magnetosphere," *Journal of Geophysical Research: Space Physics*, Vol. 87, No. A5, 1982, pp. 3481–3488. https://doi.org/10.1029/JA087iA05p03481.

[12] King, L. B., Parker, G. G., Deshmukh, S., and Chong, J. H., "Study of interspacecraft Coulomb forces and implications for formation flying," *Journal of Propulsion and Power*, Vol. 19, No. 3, 2003, pp. 497–505. https://doi.org/10.2514/2.6133.

[13] Schaub, H., Parker, G. G., and King, L. B., "Challenges and prospects of coulomb spacecraft formations," *Advances in the Astronautical Sciences*, Vol. 115, No. June, 2003, pp. 351–370.

[14] Wilson, K. T. H., 'Alvaro Romero Calvo, and Schaub, H., "Constrained Guidance for Spacecraft Proximity Operations Under Electrostatic Perturbations," *Journal of Spacecraft and Rockets*, Vol. 59, No. 4, 2022, pp. 1304–1316. https://doi.org/10.2514/1.A35162.

[15] Wilson, K., and Schaub, H., "Impact of Electrostatic Perturbations on Proximity Operations in High Earth Orbits," *Journal of Spacecraft and Rockets*, Vol. 58, No. 5, 2021, pp. 1–10. https://doi.org/10.2514/1.a35039.

[16] Wilson, K., and Schaub, H., "Constrained guidance for spacecraft proximity operations under electrostatic perturbations," *IEEE Aerospace Engineering Conference*, Big Sky, MT, 2021, pp. 1–11.

[17] Olsen, R., "Experiments in charge control at geosynchronous orbit - ATS-5 and ATS-6," *J. Spacecraft Rockets*, Vol. 22, 1985. https://doi.org/10.2514/3.25742.

[18] Stannard, P. R., Katz, I., Mandell, M. J., Cassidy, J. J., Parks, D. E., Rotenberg, M., and Steen, P. G., "Analysis of the charging of the SCATHA (P78-2) satellite," https://ntrs.nasa.gov/citations/19810018631, 1980.

[19] Purvis, C. K., Bartlett, R. O., and Deforest, S. E., "Active Control of Spacecraft Charging on ATS-5 and ATS-6," *Proceedings of the Spacecraft Charging Technology Conference*, Colorado Springs, Colorado, 1977, p. 24. URL https://ntrs.nasa.gov/citations/19780002193.

[20] Torkar, K., Nakamura, R., Tajmar, M., Scharlemann, C., Jeszenszky, H., Laky, G., Fremuth, G., Escoubet, C., and Svenes, K., "Active Spacecraft Potential Control Investigation," *Space Science Reviews*, Vol. 199, 2014. https://doi.org/10.1007/s11214-014-0049-3.

[21] Riedler, W., Torkar, K., and et al., "Active Spacecraft Potential Control," *Space Science Reviews*, Vol. 79, 1997, pp. 271–302. https://doi.org/10.1023/A:1004921614592.

[22] Torkar, K., Riedler, W., Escoubet, C. P., and et al, "Active Spacecraft Potential Control for Cluster – Implementation and First Results," *Ann. Geophys.*, 2001. https://doi.org/10.5194/angeo-19-1289-2001.

[23] Lai, S., "A critical overview on spacecraft charging mitigation methods," *IEEE Transactions on Plasma Science*, Vol. 31, No. 6, 2003, pp. 1118–1124. https://doi.org/10.1109/TPS.2003.820969.

[24] Patterson, M. J., Hamley, J. A., Sarver-Verhey, T. R., and Soulas, G. C., "Functional Testing of the Space Station Plasma Contactor," https://ntrs.nasa.gov/citations/19950016820, 1995.

[25] Burke, T. P., and Carpenter, C. B., "On the Operational Status of the ISS Plasma Contactor Hollow Cathodes," https://ntrs.nasa.gov/citations/20040110836, 2004.

[26] Hernandez-Pellerano, A., Iannello, C. J., Wollack, E. J., Wright, K. H., Garrett, H. B., Ging, A. T., Katz, I., Keith, R. L., Minow, J. I., Willis, E. M., Schneider, T. A., and Whittlesey, A. C., "International Space Station (ISS) Plasma Contactor Unit (PCU) Utilization Plan Assessment Update," https://ntrs.nasa.gov/citations/20140012780, 2014.

[27] Lai, S. T., and Miller, C., "Retarding potential analyzer: Principles, designs, and space applications," *AIP Advances*, Vol. 10, No. 9, 2020, p. 095324. https://doi.org/10.1063/5.0014266.

[28] Goembel, L., and Doering, J. P., "Instrument for measuring spacecraft potential," *Journal of spacecraft and rockets*, Vol. 35, No. 1, 1998, pp. 66–72.

[29] Pedersen, A., Lybekk, B., André, M., Eriksson, A., Masson, A., Mozer, F. S., Lindqvist, P.-A., Décréau, P. M. E., Dandouras, I., Sauvaud, J.-A., Fazakerley, A., Taylor, M., Paschmann, G., Svenes, K. R., Torkar, K., and Whipple, E., "Electron density estimations derived from spacecraft potential measurements on Cluster in tenuous plasma regions," *Journal of Geophysical Research: Space Physics*, Vol. 113, No. A7, 2008. https://doi.org/https://doi.org/10.1029/2007JA012636.

[30] Schmidt, R., Arends, H., Pedersen, A., Rüdenauer, F., and et al, "Results from Active Spacecraft Potential Control on the Geotail Spacecraft," *Journal of Geophysical Research: Space Physics*, Vol. 100, No. A9, 1996, pp. 17253–17259. https://doi.org/10.1029/95JA01552.

[31] Walker, J. D., and Schaub, H., "Electron Gun-Based Active Charge Control of Nearby Spacecraft," *IEEE Transactions on Plasma Science*, 2025, pp. 1–15. https://doi.org/10.1109/TPS.2025.3627474.

[32] Dudziak, R., Tuttle, S., and Barraclough, S., "Harpoon technology development for the active removal of space debris," *Advances in Space Research*, Vol. 56, No. 3, 2015, pp. 509–527. https://doi.org/https://doi.org/10.1016/j.asr.2015.04.012, advances in Asteroid and Space Debris Science and Technology - Part 1.

[33] Shan, M., Guo, J., and Gill, E., "Deployment dynamics of tethered-net for space debris removal," *Acta Astronautica*, Vol. 132, 2017, pp. 293–302. https://doi.org/https://doi.org/10.1016/j.actaastro.2017.01.001, URL https://www.sciencedirect.com/science/article/pii/S0094576516309961.

[34] Sharf, I., Thomsen, B., Botta, E. M., and Misra, A. K., "Experiments and simulation of a net closing mechanism for tether-net capture of space debris," *Acta Astronautica*, Vol. 139, 2017, pp. 332–343. https://doi.org/https://doi.org/10.1016/j.actaastro.2017.07.026.

[35] Kibe, S., "R&D of the Achive Removal System for Post-Mission Space Systems," *54th International Astronautical Congress of the International Astronautical Federation, the International Academy of Astronautics, and the International Institute of Space Law*, 2003. https://doi.org/10.2514/6.IAC-03-IAA.5.4.07.

[36] Nishida, S., Kawamoto, S., Okawa, Y., Terui, F., and Kitamura, S., "Space debris removal system using a small satellite," *Acta Astronautica*, Vol. 65, No. 1, 2009, pp. 95–102. https://doi.org/https://doi.org/10.1016/j.actaastro.2009.01.041.

[37] Schaub, H., and Moorer, D. F., "Geosynchronous Large Debris Reorbiter: Challenges and Prospects," *The Journal of the Astronautical Sciences*, Vol. 59, No. 1-2, 2012, pp. 161–176. https://doi.org/10.1007/s40295-013-0011-8.

[38] Schaub, H., and Sternovsky, Z., "Active Space Debris Charging for Contactless Electrostatic Disposal Maneuvers," *Advances in Space Research*, Vol. 43, No. 1, 2014, pp. 110–118. https://doi.org/10.1016/j.asr.2013.10.003.

[39] Schaub, H., and Jasper, L. E. Z., "Circular Orbit Radius Control Using Electrostatic Actuation for 2-Craft Configurations," *AAS/AIAA Astrodynamics Specialist Conference*, Girdwood, Alaska, 2011. Paper AAS 11–498.

[40] Bengtson, M., Hughes, J., and Schaub, H., "Prospects and Challenges for Touchless Sensing of Spacecraft Electrostatic Potential Using Electrons," *IEEE Transactions on Plasma Science*, Vol. 47, No. 8, 2019, pp. 3673–3681. https://doi.org/10.1109/TPS.2019.2912057.

[41] Wilson, K., and Schaub, H., "X-Ray Spectroscopy for Electrostatic Potential and Material Determination of Space Objects," *IEEE Transactions on Plasma Science*, Vol. 47, No. 8, 2019, pp. 3858–3866. https://doi.org/10.1109/TPS.2019.2910576.

[42] Bennett, T., and Schaub, H., "Contactless electrostatic detumbling of axi-symmetric GEO objects with nominal pushing or pulling," *Advances in Space Research*, Vol. 62, No. 11, 2018, pp. 2977–2987. https://doi.org/10.1016/j.asr.2018.07.021.

[43] Casale, F., Schaub, H., and Douglas Biggs, J., "Lyapunov Optimal Touchless Electrostatic Detumbling of Space Debris in GEO Using a Surface Multisphere Model," *Journal of Spacecraft and Rockets*, 2021, pp. 1–15. https://doi.org/10.2514/1.A34787.

[44] Schaub, H., and Stevenson, D., "Prospects of Relative Attitude Control Using Coulomb Actuation," *The Journal of the Astronautical Sciences*, Vol. 60, No. 3-4, 2013, pp. 258–277. https://doi.org/10.1007/s40295-015-0048-y.

[45] Walker, J., and Schaub, H., "Development of Experimental Methods for Active Charge Control using Remote Sensing Methods," *Spacecraft Charging and Technology Conference*, Avignon, France, 2024.

[46] Baglin, V., Bojko, J., Gröbner, O., Henrist, B., Hilleret, N., Scheuerlein, C., and Taborelli, M., "The Secondary Electron Yield of Technical Materials and its Variation with Surface Treatments," *7th European Particle Accelerator Conference*, 2000.

[47] Lundgreen, P., and Dennison, J. R., "Strategies for Determining Electron Yield Material Parameters for Spacecraft Charge Modeling," *Space Weather*, Vol. 18, No. 4, 2020. https://doi.org/10.1029/2019SW002346.

[48] Sanders, N. L., and Inouye, G. T., "Secondary emission effects on spacecraft charging: Energy distribution considerations," *Spacecraft Charging Technology - 1978*, NASA, 1979, pp. 747–755.

[49] Prokopenko, S., and Laframboise, J., "High-voltage differential charging of geostationary spacecraft," *Journal of Geophysical Research: Space Physics*, Vol. 85, No. A8, 1980, pp. 4125–4131. https://doi.org/10.1029/JA085iA08p04125.

[50] Darlington, E. H., and Cosslett, V. E., “Backscattering of 0·5-10 keV electrons from solid targets,” *Journal of Physics D: Applied Physics*, Vol. 5, No. 11, 1972, p. 1969. https://doi.org/10.1088/0022-3727/5/11/305, URL https://doi.org/10.1088/0022-3727/5/11/305.

[51] Laframboise, J. G., and Kamitsuma, M., “The threshold temperature effect in high voltage spacecraft charging,” *Proceedings of Air Force Geophysics Workshop on Natural Charg- ing of Large Space Structures in Near Earth Polar Orbit*, 1983, pp. 293–308.

[52] Bengtson, M. T., Wilson, K. T., and Schaub, H., “Experimental Results of Electron Method for Remote Spacecraft Charge Sensing,” *Space Weather*, Vol. 18, No. 3, 2020. https://doi.org/10.1029/2019SW002341.

[53] Lamoureux, M., and Charles, P., “General deconvolution of thin-target and thick-target Bremsstrahlung spectra to determine electron energy distributions,” *Radiation Physics and Chemistry*, Vol. 75, No. 10, 2006, pp. 1220–1231. https://doi.org/https://doi.org/10.1016/j.radphyschem.2006.06.006.